Optimization-based Position Sensorless Finite Control Set Model Predictive Control for IPMSMs

Shamsuddeen Nalakath, *Student Member, IEEE,* Yingguang Sun, *Member, IEEE,* Matthias Preindl, *Member, IEEE,* and Ali Emadi, *Fellow, IEEE*

***Abstract*—This paper presents nonlinear optimization based position and speed estimation scheme for IPMSM drives with arbitrary signal injection generated by inherent switching ripples associated with finite control set model predictive control (FCSMPC). The existing standard sensorless techniques are not suitable for FCSMPC which applies voltage vectors directly to an electrical machine without a modulator. The proposed method optimizes the nonlinear cost function derived from the standard IPMSM model with respect to position and speed at every sampling interval. This method can be applied to any type of signal injection and hence an ideal candidate for sensorless FCSMPC. In this method, the signal injection is needed only to generate persistent excitation to maintain the observability at low speeds. A strong persistent excitation is always present with FCSMPC except at standstill where the control applies null vector when the reference currents are zero. This situation is overcome in this paper by introducing a small negative d axis current at standstill. Thus, the proposed method can estimate the position and speed over a wide speed range starting from standstill to the rated speed without a changeover or additional signal injection. This paper also presents detailed convergence analysis and proposes a compensator for standstill operation that prevents converging to saddle and symmetrical solutions, and therefore also eliminates the well known ambiguity of π rad in position estimation. The performance of the proposed sensorless scheme is experimentally verified for a wide range of operating conditions.**

***Index Terms*—Permanent magnet machines, sensorless control, predictive control, optimization, cost function and Newton method.**

I. Introduction

The model predictive control (MPC) was originally developed for process industries with a slow sampling rate, however, it has been recently employed in power electronics and motor drive applications with the support of fast, modern processors [1]. The MPC with finite control set (FCSMPC) is drawing more attention in motor drive applications as compared to the continuous MPC as the latter needs more computational resources to solve the nonlinear optimization problem [2][3]. In FCSMPC, the cost function is minimized for a finite number of control inputs which are essentially inverter switching sequences for the motor drive applications. One of the well established examples of FCSMPC in motor control is model predictive direct torque control (MPDTC) in which torque and flux components are controlled separately in $\alpha\beta$ frame similar to the conventional direct torque control [4][5][6]. In another version of FCSMPC, the currents are controlled in dq frame to perform field oriented control, in which the voltage vectors are chosen to minimize the error between reference and predicted currents [7][8]. The control in dq frame simplifies the mathematical formulation and becomes convenient to add any objective to the cost function such as MTPA and loss minimization [8], however control realization in this reference frame requires the position information.

The standstill and low-speed position estimations are challenging as the system is not observable unless there is a persistent excitation into the system [9]. The persistent excitation is generally established by injecting high-frequency signals such as sinusoidal, square, arbitrary and pulse vector into the system. The responses of these injected signals are utilized in extracting the position information in the standard position estimation techniques. For instance, the demodulation based techniques are applied to periodic continuous injection like sinusoidal and square waves, and the current derivative model based methods are employed for pulse vector injection [10]-[14]. The aforementioned techniques can not be directly applied for the sensorless FCSMPC as it does not have any modulator to superimpose the injected signal with the fundamental excitation. There is an attempt to estimate the position from the high frequency reactive power with demodulation technique in [15], however the wide varying nature of the arbitrary injection frequency associated with FCSMPC causes difficulty in locking the filter and phase locked loop (PLL) parameters. The cost function of the FCSMPC is modified to superimpose the high-frequency sinusoidal signal along with the control vectors in [16]. However, differentiating the responses between the superimposed signal and the inherent high-frequency vector is challenging as this method relies on the standard demodulation.

The model based methods appear to be an effective solution in literature for sensorless FCSMPC especially at standstill and at low-speeds. A model based position and speed estimation scheme with a second order observer consisting of a PLL and feed forward loop is presented in [17]. This method works for a wide speed range except at very low speed close to the standstill as there are transients in the convergence. A model based method for FCSMPC with specially simplified model equations is introduced in [18]. The results are promising except for the 12 electrical degree oscillations in position at

S. Nalakath and A. Emadi are with the Department of Electrical and Computer Engineering, McMaster University, Hamilton, ON L8S 4L8, Canada, (e-mail: nalakas@mcmaster.ca; emadi@mcmaster.ca).

Y. Sun was with the Department of Electrical and Computer Engineering, McMaster University, Hamilton, ON L8S 4L8, Canada, (e-mail: suny77@mcmaster.ca).

M. Preindl is with the Department of Electrical Engineering, Columbia University in the City of New York, New York, NY 10027, USA, (e-mail: matthias.preindl@columbia.edu)

nominal load. The reduced order extended Kalman filter is employed to estimate the position and speed in [19]. This method works for low and high speeds, however there is a position error at steady state up to 22 electrical degree. The sensorless scheme based on extended mean admittance is presented in [20]. The position and speed show phase advances in this method due to load-dependent saliency displacement, and the oscillation in position at standstill is about 10 electrical degree. The model based methods for medium and high speeds are well established in literature and it is less challenging as there is a strong back emf component which provides position information. In contrast, it is still an open problem for refinements for FCSMPC at low speeds.

In [21], nonlinear optimization based technique is applied to estimate the position and speed for an IPMSM drive with vector control and sinusoidal injection. This paper applies the similar technique to IPMSM drive with the arbitrary signal injection generated by inherent switching ripples associated with FCSMPC. The influence of switching ripples at different operating points on the accuracy of the estimation are analyzed with experimental results to verify the suitability of the proposed method in this paper. The detailed convexity analysis with the help of leading principle minors is also included. This analysis provides insights into saddle and symmetrical solutions and helped to propose a compensator for standstill operation that prevents converging into those undesirable solutions. This compensator also functions as an integrated polarity detector thereby avoiding inclusion of any additional techniques to eliminate the well known ambiguity of π rad in position estimation. The position estimation at standstill condition for FCSMPC is problematic as the control applies null vector when the current references are zero causing nonexistence of persistent excitation. It should be noted that the standstill performance of sensorless FCSMPC is not presented in [15]-[18]. In [19] and [20], there is a high frequency injection for estimating the position at standstill with no load. In this paper, a small constant negative d axis reference current is applied only at standstill to produce the switching ripples which enables position estimation even at no load.

The proposed sensorless technique presented in this paper is capable of estimating position and speed over a wide speed range starting from standstill to the rated speed without any changeover or additional signal injection. This technique optimizes the nonlinear cost function derived from the standard IPMSM model in the estimated reference frame ($\delta\gamma$) with respect to position error and speed. The optimization in $\delta\gamma$ is equivalent to $\alpha\beta$ where the former is chosen only for the sake of simplicity in the convergence analysis. Newton minimization along with golden section line search is employed as the nonlinear optimization solver in this paper. The optimal position error solution from the optimizer is fed to a standard PLL to track the position. The experimental results are presented for speed-torque reversals, and speed sweep from standstill to high speed to verify the performance of the proposed sensorless FCSMPC.

The rest of the paper is organized as section II describes the details of formulating the nonlinear optimization, and in section III, the convergence analysis is discussed. Section IV presents the proposed compensator for saddle and symmetrical solutions and section V provides the details of the sensorless FCSMPC scheme. The experimental setup and the results are presented in section VI, and section VII concludes the paper.

II. Nonlinear Optimization

The cost function is formulated in the estimated reference frame ($\delta\gamma$) which rotates with estimated velocity ($\hat{\omega}$) and displaced from the dq frame with an estimated angle difference $\hat{\vartheta}$. The mathematical model of IPMSM in $\delta\gamma$ is essentially derived from the machine model in dq, i.e.

$$\tilde{\mathbf{v}}_{\mathbf{dq}} = \mathbf{L}_{\mathbf{dq}}\dot{\mathbf{i}}_{\mathbf{dq}} + \mathbf{T}\mathbf{L}_{\mathbf{dq}}\omega\mathbf{i}_{\mathbf{dq}} + \mathbf{q}\omega\psi. \tag{1}$$

where $\tilde{\mathbf{v}}_{\mathbf{dq}} = \mathbf{v}_{\mathbf{dq}} - R\mathbf{i}_{\mathbf{dq}}$, is the voltage vector in dq compensated with resistive drops $R\mathbf{i}_{\mathbf{dq}}$, $\mathbf{i}_{\mathbf{dq}}$ is the current vector in dq, $\mathbf{T} = [[0,1]', [-1,0]']$, $\mathbf{L}_{\mathbf{dq}} = [[L_d, 0]', [0, L_q]']$, L_d and L_q are d and q inductances, ω is electrical angular speed, ψ is permanent magnet flux linkage, and $\mathbf{q} = [0,1]'$.

The IPMSM model in $\delta\gamma$ frame, found by transforming $\tilde{\mathbf{v}}_{\mathbf{dq}} = \mathbf{P}\tilde{\mathbf{v}}_{\delta\gamma}$, $\mathbf{i}_{\mathbf{dq}} = \mathbf{P}\mathbf{i}_{\delta\gamma}$, and $\dot{\mathbf{i}}_{\mathbf{dq}} = \mathbf{P}\dot{\mathbf{i}}_{\delta\gamma} - \mathbf{T}\mathbf{P}\omega\mathbf{i}_{\delta\gamma}$, is

$$\tilde{\mathbf{v}}_{\delta\gamma} = \mathbf{L}_{\delta\gamma}\dot{\mathbf{i}}_{\delta\gamma} + \mathbf{T}\mathbf{L}_{\delta\gamma}\hat{\omega}\mathbf{i}_{\delta\gamma} + \tilde{\mathbf{q}}\hat{\omega}\psi. \tag{2}$$

where $\mathbf{P} = [[\cos\hat{\vartheta},\ -\sin\hat{\vartheta}]',\ [\sin\hat{\vartheta},\ \cos\hat{\vartheta}]']$, $\mathbf{L}_{\delta\gamma} = \tilde{\mathbf{P}}L_{\Delta} + L_{\Sigma}\mathbf{I}$, $L_{\Delta} = (L_d - L_q)/2$, $L_{\Sigma} = (L_d + L_q)/2$, $\tilde{\mathbf{P}} = [[\cos 2\hat{\vartheta},\ \sin 2\hat{\vartheta}]',\ [\sin 2\hat{\vartheta},\ -\cos 2\hat{\vartheta}]']$, $\mathbf{I} = [[1,0]',\ [0,1]']$, and $\tilde{\mathbf{q}} = [-\sin\hat{\vartheta},\ \cos\hat{\vartheta}]'$. Equation (2) can be expressed as a function, i.e.

$$\mathbf{h} = \mathbf{L}_{\delta\gamma}\dot{\mathbf{i}}_{\delta\gamma} + \mathbf{T}\mathbf{L}_{\delta\gamma}\hat{\omega}\mathbf{i}_{\delta\gamma} + \tilde{\mathbf{q}}\hat{\omega}\psi - \tilde{\mathbf{v}}_{\delta\gamma}. \tag{3}$$

The function (3) is discretized by the forward Euler method and the proposed cost function is

$$f_k = \|\mathbf{h_k}\|_2^2 + \kappa_1(\hat{\vartheta}_k - \hat{\vartheta}_{k-1})^2 + \kappa_2(\hat{\omega}_k - \hat{\omega}_{k-1})^2, \tag{4}$$

where $\mathbf{h_k}$ is the discrete function of (3), $\|\mathbf{h_k}\|_2^2$ is the square of the two norm of $\mathbf{h_k}$, κ_1 and κ_2 are the heuristically tuned constants. The second and the third terms in the cost function are added to reduce the ripples in optimal solution that originates from the noise in the current feedback measurements. The cost function (4) is optimized with respect to $\hat{\vartheta}$ and $\hat{\omega}$ at every sampling interval.

$$\underset{\hat{\vartheta},\ \hat{\omega}}{\text{minimize}} f_k.$$

This paper employs Newton minimization along with golden-section line search as the optimization solver. Newton's method guarantees quadratic convergence as long as the convergence trajectory is confined within the convex region, which can be achieved with a warm-start initialization and by incorporating a line search to ensure a descent direction for each iteration [22]. The iterative optimization algorithm is carried out within a sampling interval as

$$\begin{cases} \Delta\mathbf{x}_k^n = -\frac{\mathbf{J}(\mathbf{x}_k^{n-1})}{\mathbf{H}(\mathbf{x}_k^{n-1})} \\ \underset{\xi}{\text{minimize}} f(\mathbf{x}_k^{n-1} + \xi\Delta\mathbf{x}_k^n) \\ \mathbf{x}_k^n = \mathbf{x}_k^{n-1} + \xi\Delta\mathbf{x}_k^n \end{cases} \tag{5}$$

where $\mathbf{x}_k = [\hat{\vartheta}_k, \hat{\omega}_k]'$, $\Delta\mathbf{x}_k^n$ is Newton direction of the k^{th} sample and n^{th} Newton iteration, $\mathbf{H}$ is Hessian, and $\mathbf{J}$ is Jacobian. The line search step length (ξ) is found by the intermediate optimization (golden-section [23]), which essentially finds ξ resulting from

$$f(\mathbf{x}_k^{n-1} + \xi\Delta\mathbf{x}_k^n) < f(\mathbf{x}_k^{n-1}).$$

The steps in (5) are repeated until $\mathbf{J}(\mathbf{x}_k) \leq \eta$ (an acceptable minimum). The value of η is chosen to reduce the number of iterations without compromising on the accuracy of the solution. The number of iterations is further reduced in this application as there is always a warm initialization except for the initial sample. This is true from the fact that, the initialization for the k^{th} sample is the solution from $k-1^{th}$ sample, and the variations between these adjacent samples are marginal. It is also worthwhile to note that a compensator is proposed in this paper for the initial sample at the start-up to avoid wrong convergence.

III. Convergence Analysis

There is a global minimum if the cost function is convex and the solution converges to this minimum as long as the convergence trajectory is confined within the convex region. Therefore, analyzing the convex region is the fundamental part of the convergence analysis. One of the approaches to find the convex region of the cost function is with the help of the leading principal minors of its Hessian matrix [24]. This approach is convenient in developing analytical conditions for the convexity. The Hessian of the cost function (4) is

$$\mathbf{H} = \begin{bmatrix} 2\mathbf{h}'\mathbf{h}_{\hat{\vartheta}\hat{\vartheta}} + 2\mathbf{h}'_{\hat{\vartheta}}\mathbf{h}_{\hat{\vartheta}} + 2\kappa_1, & 2\mathbf{h}'\mathbf{h}_{\hat{\vartheta}\hat{\omega}} + 2\mathbf{h}'_{\hat{\vartheta}}\mathbf{h}_{\hat{\omega}} \\ 2\mathbf{h}'\mathbf{h}_{\hat{\vartheta}\hat{\omega}} + 2\mathbf{h}'_{\hat{\vartheta}}\mathbf{h}_{\hat{\omega}}, & 2\mathbf{h}'_{\hat{\omega}}\mathbf{h}_{\hat{\omega}} + 2\kappa_2 \end{bmatrix} \tag{6}$$

where $\mathbf{h}_{\hat{\vartheta}}$, $\mathbf{h}_{\hat{\vartheta}\hat{\vartheta}}$, $\mathbf{h}_{\hat{\omega}}$, and $\mathbf{h}_{\hat{\vartheta}\hat{\omega}}$ are the first and second order derivatives of $\mathbf{h}$ with respect to $\hat{\vartheta}$ and $\hat{\omega}$, and their expressions are

$$\begin{aligned}
\mathbf{h}_{\hat{\vartheta}} &= 2L_{\triangle}\mathbf{T}(\tilde{\mathbf{P}}\dot{\mathbf{i}}_{\delta\gamma} + \mathbf{T}\tilde{\mathbf{P}}\hat{\omega}\mathbf{i}_{\delta\gamma}) + \psi\hat{\omega}\mathbf{T}\tilde{\mathbf{q}} \\
\mathbf{h}_{\hat{\vartheta}\hat{\vartheta}} &= 2\mathbf{T}\mathbf{h}_{\hat{\vartheta}} \\
\mathbf{h}_{\hat{\omega}} &= \mathbf{T}\mathbf{L}_{\delta\gamma}\mathbf{i}_{\delta\gamma} + \tilde{\mathbf{q}}\psi \\
\mathbf{h}_{\hat{\vartheta}\hat{\omega}} &= 2L_{\triangle}\mathbf{T}\mathbf{T}\tilde{\mathbf{P}}\mathbf{i}_{\delta\gamma} + \psi\mathbf{T}\tilde{\mathbf{q}}
\end{aligned}$$

and the Jacobian is

$$\mathbf{J} = [2\mathbf{h}'\mathbf{h}_{\hat{\vartheta}} + 2\kappa_2(\hat{\vartheta} - \hat{\vartheta}_i), 2\mathbf{h}'\mathbf{h}_{\hat{\omega}} + 2\kappa_2(\hat{\omega} - \hat{\omega}_i)]' \tag{7}$$

where $\hat{\vartheta}_i$ and $\hat{\omega}_i$ are the initial values (from the preceding sample).

Hessian (6) has two leading principal minors

$$\begin{aligned} m_1 &= h_{11} \\ m_2 &= |\mathbf{H}| \end{aligned} \tag{8}$$

where h_{11} is the first element and $|\mathbf{H}|$ is the determinant of $\mathbf{H}$.

The required conditions for the convexity are [24]

$$m_1 > 0 \text{ and } m_2 > 0 \tag{9}$$

The values of $\hat{\vartheta}$ and $\hat{\omega}$ at the boundary of the convexity region can be numerically found by solving $m_1 = 0$ and $m_2 = 0$. In addition to those actual values, this paper presents the simplified analytical expressions for the leading principal minors in order to arrive the conditions for the convexity. The simplification is carried out only for the sake of convergence analysis, and the actual Hessian (6) and the cost function (4) are used for optimization. The simplification is carried out by neglecting the less significant terms from the original expressions for low speed and high speed cases.

A. High Speed Convergence Analysis

The back emf is the major component in the original leading principal minors (8) at high speed and therefore the current terms ($\dot{\mathbf{i}}_{\delta\gamma}$, $\mathbf{i}_{\delta\gamma}$) are neglected to find the simplified expressions for analyzing the convex region. Thus, the first simplified principle minor is derived as

$$m_1^h = 2\psi\hat{\omega}|\mathbf{v}_{\delta\gamma}|\cos(\hat{\vartheta} + \tan^{-1}\frac{v_\delta}{v_\gamma}), \tag{10}$$

where superscript h indicates high speed, and the first convexity condition by applying $m_1^h > 0$ is

$$\left.\begin{aligned} \tan^{-1}\tfrac{v_\delta}{v_\gamma} - \tfrac{\pi}{2} < \\ \tan^{-1}\tfrac{v_\delta}{v_\gamma} - \tfrac{\pi}{2} > \end{aligned}\right\} \hat{\vartheta} \begin{cases} < \tan^{-1}\frac{v_\delta}{v_\gamma} + \frac{\pi}{2} & \text{for } \hat{\omega} > 0 \\ > \tan^{-1}\frac{v_\delta}{v_\gamma} + \frac{\pi}{2} & \text{for } \hat{\omega} < 0 \end{cases} \tag{11}$$

Similarly the second principle minor is derived as

$$m_2^h = 4\psi^2\left[\frac{m_1}{2} - |\mathbf{v}_{\delta\gamma}|^2\sin(\hat{\vartheta} + \tan^{-1}\frac{v_\delta}{v_\gamma})^2\right] \tag{12}$$

and the second convexity condition by applying $m_2^h > 0$ is

$$\omega \begin{cases} > \frac{|\mathbf{v}_{\delta\gamma}|\sin(\hat{\vartheta}+\tan^{-1}\frac{v_\delta}{v_\gamma})^2}{2\psi\cos(\hat{\vartheta}+\tan^{-1}\frac{v_\delta}{v_\gamma})}, & \text{for } d^h > 0 \\ < \frac{|\mathbf{v}_{\delta\gamma}|\sin(\hat{\vartheta}+\tan^{-1}\frac{v_\delta}{v_\gamma})^2}{2\psi\cos(\hat{\vartheta}+\tan^{-1}\frac{v_\delta}{v_\gamma})}, & \text{for } d^h < 0, \end{cases} \tag{13}$$

where d^h is the denominator $2\psi\cos(\hat{\vartheta} + \tan^{-1}\frac{v_\delta}{v_\gamma})$ in (13).

The convex region at high speed is plotted based on the approximated (11, 13) and the original conditions (8) for the reference IPM machine (see Table I for the machine details) along with its cost function at 314 rad/s (600 rpm), $i_q = 2$ A, $i_d = 0$ A, and $\dot{i}_d = \dot{i}_q = 0$ A in Fig. 1. It is shown that the difference between the original and the approximated convex regions is negligible. Moreover, the cost function is odd symmetric and has four equilibrium solutions

$$\left| \begin{array}{ll} s_1 : (\hat{\vartheta}_o, \hat{\omega}_o) & s_3 : (\hat{\vartheta}_o + \dfrac{\pi}{2}, 0) \\ s_2 : (\hat{\vartheta}_o - \pi, -\hat{\omega}_o) & s_4 : (\hat{\vartheta}_o - \dfrac{\pi}{2}, 0). \end{array} \right.$$

The solution s_1 is the optimal solution and $\hat{\vartheta}_o$ and $\hat{\omega}_o$ are the optimal values of $\hat{\vartheta}$ and $\hat{\omega}$. The solutions s_3 and s_4 at $\hat{\omega} = 0$ are saddle solutions. The symmetrical solution s_2 is shifted by π rad from the optimal solution. The non-convex region in Fig. 1 is not concave ($m_1 < 0$, and $m_2 > 0$) [24] and therefore it is a saddle region where neither minimum nor maximum exists.

Fig. 1 also shows the convergence trajectories of Newton iterations starting from different initial conditions. The intermediate trajectories by line search is omitted in the plot. The trajectories with their starting points in the convex region are

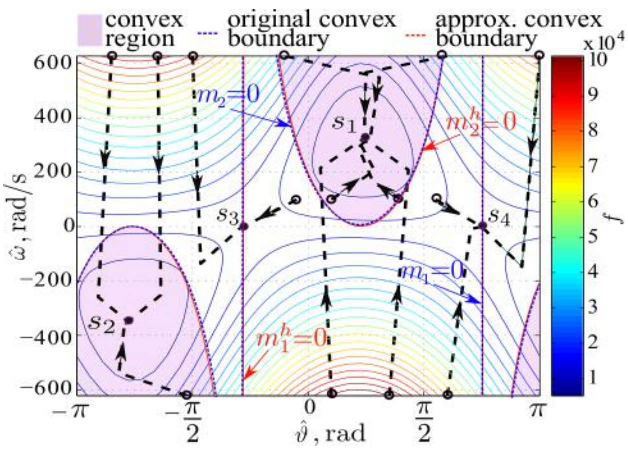

Figure 1. The contour plot of the cost function (f), convex region, and the convergence trajectories for the high speed case.

converged to the optimal solution. The iterations with initial $\hat{\omega}$ having opposite sign as compared to $\hat{\omega}_o$ also converge to the optimal solution as long as the initial $\hat{\vartheta}$ is close to $\hat{\vartheta}_o$. Otherwise, the iterations converge to either symmetrical or a saddle solution (s_3/s_4) depending on the location of the initial condition. All the trajectories in Fig. 1 are converged within three Newton and six line search iterations.

B. Low Speed Convergence Analysis

The current derivative term is the major component in the original leading principle minors (7) at low speed because its value is kept high (by signal injection or by inherent switching ripples) to provide persistent excitation to meet the well known observability condition for IPMSMs [9]. Thus, it enables to neglect the terms with $\mathbf{i}_{\delta\gamma}$ from the original leading principal minors to find the simplified expressions for analyzing the convex region. The first simplified leading principle minor for the low speed case is

$$m_1^l = 2\psi\hat{\omega}(a+b) - 8L_2(c - L_\Sigma d), \tag{14}$$

where,

$$a = |\mathbf{v}_{\delta\gamma}|\cos(\hat{\vartheta} + \tan^{-1}\frac{v_\delta}{v_\gamma})$$
$$b = |\dot{\mathbf{i}}_{\delta\gamma}|\cos(\hat{\vartheta} + \tan^{-1}\frac{\dot{i}_\delta}{\dot{i}_\gamma})(L_\Delta - L_\Sigma)$$
$$c = |\dot{\mathbf{i}}_{\delta\gamma}||\mathbf{v}_{\delta\gamma}|\cos(\hat{\vartheta} + \tan^{-1}\frac{v_\delta}{v_\gamma} + \tan^{-1}\frac{\dot{i}_\delta}{\dot{i}_\gamma})$$
$$d = |\dot{\mathbf{i}}_{\delta\gamma}|\cos(2\hat{\vartheta} + 2\tan^{-1}\frac{\dot{i}_\delta}{\dot{i}_\gamma})$$

where superscript l indicates low speed, and the first convexity condition by applying $m_1^l > 0$ is

$$\omega \begin{cases} > \frac{8L_\Delta(c-L_\Sigma d)}{2\psi(a+b)}, & \text{for } d^l > 0 \\ < \frac{8L_\Delta(c-L_\Sigma d)}{2\psi(a+b)}, & \text{for } d^l < 0, \end{cases} \tag{15}$$

where d^l is the denominator $2\psi(a+b)$ in (15). Similarly the simplified expression for the second leading principle minor for the low speed case is

$$m_2^l = 2\psi^2\left[m_1 - 2(a+b)^2\right], \tag{16}$$

and the second convexity condition by applying $m_2^l > 0$ is

$$\omega \begin{cases} > \frac{8L_\Delta(c-L_\Sigma d)+2(a+b)^2}{2\psi(a+b)}, & \text{for } d^l > 0 \\ < \frac{8L_\Delta(c-L_\Sigma d)2+(a+b)^2}{2\psi(a+b)}, & \text{for } d^l < 0 \end{cases} \tag{17}$$

According to the conditions (15) and (17), the cost function for the surface permanent magnet machines is not convex at $\hat{\omega} = 0$ as $L_\Delta = 0$. For IPMSMs, at least one current derivative must be nonzero to maintain the convexity.

The convex region at low speed with the help of approximated (15, 17) and the original (8) conditions along with the cost function for the reference IPMSM at 0 rad/s, $\dot{i}_\gamma = 10000$A/s, $\dot{i}_\gamma = 1000$ A/s, $i_\delta = 0$ A, and $i_\gamma = 2$ A are plotted in Fig. 2. The difference between the approximated and the original convex regions is negligible. Moreover, the convex boundaries by two approximated conditions (15) and (17) are overlapped. The cost function is odd symmetric and has four equilibrium solutions

$$\left| \begin{array}{ll} s_1 : (\hat{\vartheta}_o, \hat{\omega}_o) & s_3 : (\hat{\vartheta}_o + \frac{\pi}{2}, \hat{\omega}_s) \\ s_2 : (\hat{\vartheta}_o - \pi, -\hat{\omega}_o) & s_4 : (\hat{\vartheta}_o - \frac{\pi}{2}, -\hat{\omega}_s), \end{array} \right.$$

where $\hat{\omega}_s$ is the angular speed at the saddle solutions s_3 and s_4. The solution s_1 is the optimal solution and s_2 is the symmterical solution shifted by π rad from $\hat{\vartheta}_o$.

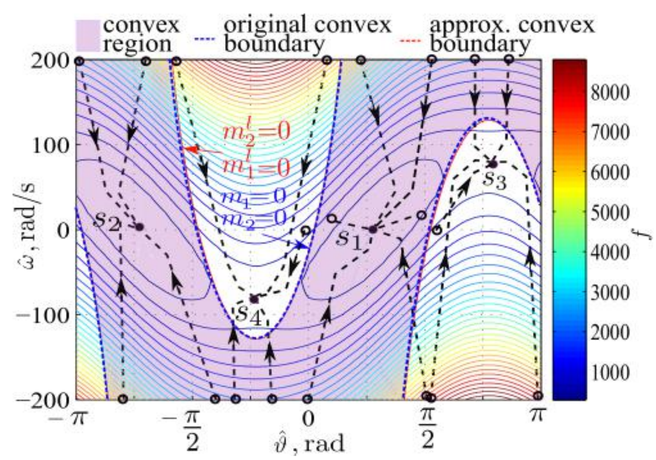

Figure 2. The contour plot of the cost function (f), convex region, and the convergence trajectories for the low speed case.

Fig. 2 also shows Newton trajectories without intermediate solutions by line search. All the trajectories started within the convex region are converged to the optimal solution except those near the saddle or symmetrical points as shown in Fig. 2. Similar to the high speed case all the trajectories are converged within three Newton and six line search iterations, and the non-convex region is not concave but the saddle region.

IV. Compensator Design

The position error solution by nonlinear optimization is more susceptible to saddle and symmetrical convergence at the start-up of the operation as the initial conditions are unknown. If the initial speed is kept as zero, which is true at the start-up, the narrow convex region at $\hat{\omega} = 0$ also increases the possibility of wrong convergence as in Fig. 2. Therefore, this paper focuses on designing a compensator only for the start-up from standstill. Once the correct standstill position is known, then the compensator is removed for the further operation. The compensation for the symmetrical solution is essentially the compensation for the opposite magnetic polarity and therefore the proposed compensator is also an integrated polarity detector.

If the solution has converged to saddle points at standstill, then the speed solution is nonzero according to Fig. 2. If the speed solution is zero then the solution is either optimal or symmetrical. The angular distances from the symmetrical and the saddle solutions to the optimal solution are π and $\frac{\pi}{2}$ respectively. The compensator is designed based on these convergence characteristics. The proposed compensator, as illustrated in Fig. 3(a) detects whether the speed solution is zero, positive or negative. If the speed is positive/negative then the algorithm chooses path-2/path-3 and subtracts/adds $\frac{\pi}{2}$ to correct the saddle solution to the optimal solution. The algorithm chooses path-1 if the speed is zero then adds $\frac{\pi}{2}$ to force the solution to a saddle point and runs the algorithm once again to move the saddle solution to the optimal solution.

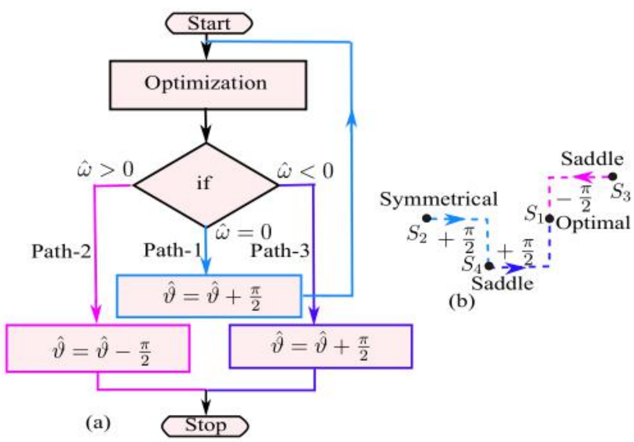

Figure 3. (a) Compensation flow chart, and (b) compensation trajectory.

V. Sensorless FCSMPC Scheme

The complete block diagram of the sensorless FCSMPC scheme is depicted in Fig. 4. The scheme consists of the non-linear optimization based estimator which provides estimated position and speed to FCSMPC. FCSMPC generates voltage vector which produces minimum cost and then applies to the IPMSM via voltage source inverter (VSI). The details of the estimator and FCSMPC are provided in the following sections.

A. Position and Speed Estimator

The nonlinear optimization of the cost function (4) in $\delta\gamma$ frame finds the optimal position difference $\hat{\vartheta}_o$. The estimated

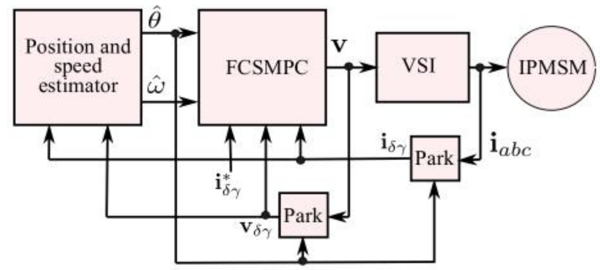

Figure 4. The complete block diagram of the sensorless FCSMPC.

position $\hat{\theta}$ is found by feeding $\hat{\vartheta}_o$ into a PLL as shown in Fig. 5. The compensator for saddle and symmetrical solutions is executed only at the start-up from standstill and it is disconnected for the remaining operation. The estimated speed $\hat{\omega}$ is the output of the discrete filter.

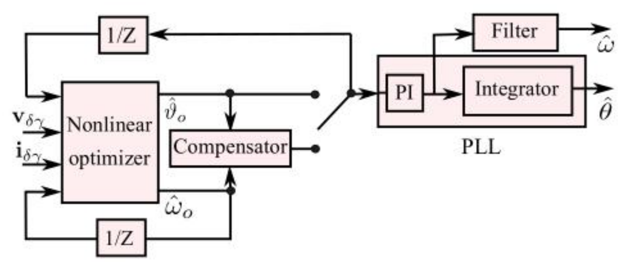

Figure 5. Nonlinear optimization based position and speed estimator.

B. FCSMPC

The finite control set model predictive control for the proposed sensorless scheme is performed in $\delta\gamma$ frame. Therefore, the voltages and the feedback currents from abc frame are transformed into $\delta\gamma$ frame based on the estimated position $\hat{\theta}$ as shown in Fig. 6. The transformed current $\mathbf{i}_{\delta\gamma,k}$ is compensated for one sampling delay to account for the time difference between the measurement and the application of the control action [18]. The compensated current $\mathbf{i}_{\delta\gamma,k+1}$ is found from the discrete IPMSM model (2). The seven predicted currents $\mathbf{i}^n_{\delta\gamma,k+2}$ corresponding to seven voltage vectors $\mathbf{v}^n$, where $n = [1, 2, ..7]$, are also found from the IPMSM model. The seven voltage vectors correspond to seven states of the two level inverter. The cost function for the FCSMPC is the difference between the reference currents and the predicted currents, i.e.

$$f^n_c = (\mathrm{i}^*_\delta - \mathrm{i}^n_{\delta,k+2})^2 + (\mathrm{i}^*_\gamma - \mathrm{i}^n_{\gamma,k+2})^2. \tag{18}$$

where i^*_δ and i^*_γ are the reference currents. The voltage vector which produces the minimum cost is then applied to IPMSM via voltage source inverter.

VI. Experimental Validation

The proposed position estimation technique was experimentally validated for the reference IPMSM with the details given in Table I. The tests were conducted in the motor dyno which is shown in Fig. 7. The dyno consists of an

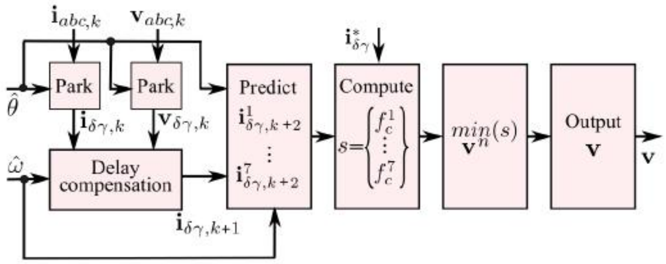

Figure 6. FCSMPC scheme.

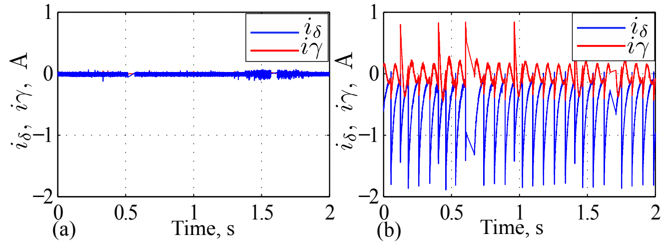

Figure 8. The measured $\delta\gamma$ currents at standstill: (a) $i_\delta^* = 0$ A and $i_\gamma^* = 0$ A, and (b) $i_\delta^* = -1$ A and $i_\gamma^* = 0$ A.

induction motor with the Yaskawa drive. The motor control and position estimator algorithms for the reference IPMSM are implemented in MicroAutobox II. The controllers are configured to run the IM in speed control and the IPMSM in current control. The sampling frequency is kept at 10kHz.

Table I
THE DETAILS OF THE REFERENCE IPMSM

Details	Values
Number of poles	10
Rated current	9.4 A
Rated torque	29.7 Nm
Rated speed	700 rpm
d axis inductance	11 mH
q axis inductance	14.3 mH
PM flux linkage	333.3 mWb
Stator resistance	400 mΩ
DC link voltage	300 V

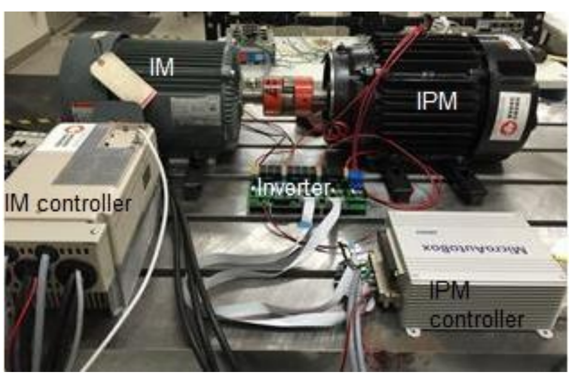

Figure 7. Motor dyno setup.

A. Standstill Performance

The FCSMPC injects null voltage vector at standstill when the reference currents (i_δ^* and i_γ^*) are zero and essentially stops persistent excitation. In this situation the position becomes not observable [9]. In order to overcome this situation, a negative reference current (-1 A) is applied in δ axis. The measured currents at standstill with zero reference currents and only -1 A in δ axis are shown in Fig. 8 (a) and (b) respectively. The current measurement with zero reference currents contains only noise in (a) and that with $i_\delta^* = -1$ A shows the switching ripples in (b).

The position estimation at standstill with $i_\delta^* = -1$ A and $i_\gamma^* = 0$ A is shown in Fig. 9. The position error ($\hat{\vartheta}_o$) is 1.5 rad at the open loop and the estimated position ($\hat{\theta}$) is zero as the PLL is not in action. At the closed loop, the PLL takes the position error to zero irrespective of whether it is an optimal, saddle or symmetrical solutions however the wrong convergence can be reflected in the estimated position $\hat{\theta}$. In Fig. 9 (a), the solution is a symmetrical solution as there is a π shift from the actual position (θ_{act}). At 4 s, the compensator comes into action as shown in Fig. 9 (b) and the estimated position converges to the actual position. The time 4 s to start the compensation is chosen only for the demonstration however in the actual sensorless operation the compensation begins at the start-up.

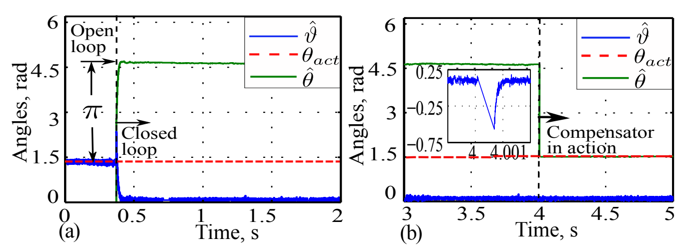

Figure 9. Position estimation at standstill with $i_\delta^* = -1$ A and $i_\gamma^* = 0$ A: (a) open loop till 0.4 s and then closed loop (b) the compensator in action at 4 s.

B. Speed Transient Performance

The speed transient performance of the proposed nonlinear optimization based sensorless FCSMPC is validated by conducting the speed reversal and sweep tests. The performance of the speed reversal tests at 50 rpm with no load and 50% rated load are shown in Fig. 10. The steady state position error for the case of no load is 0.03 rad and that for the half rated load is 0.14 rad. The increased error with loading attributes to the deviation from the nominal inductances by saturation. The steady state position error values from both the tests are close to the nonlinear optimization based sensorless vector control presented in [21]. The transient performance at no load case is also comparable with [21] however the position error at half the rated load decreases at the transition period. This is due to the fact that the estimated position while generating in Fig. 10(e-h) is below the actual position, and when the machine transitions to motoring, the estimated position moves close to the actual as the estimation response is slower than the system. The same test at 50 rpm and half the rated load is repeated for the transition from motoring to generating with a positive load current as shown in Fig. 11(a-b). For this case, the magnitude of the steady state position error is as same as in Fig. 10(e) however the estimated position is higher than the actual. Therefore, when the machine slows down at the transition to generation the actual position falls further below the estimated position causing higher position error at the transient. In both the cases the nonlinear optimizer estimates the position error promptly and PLL takes the estimated position back to its steady state value.

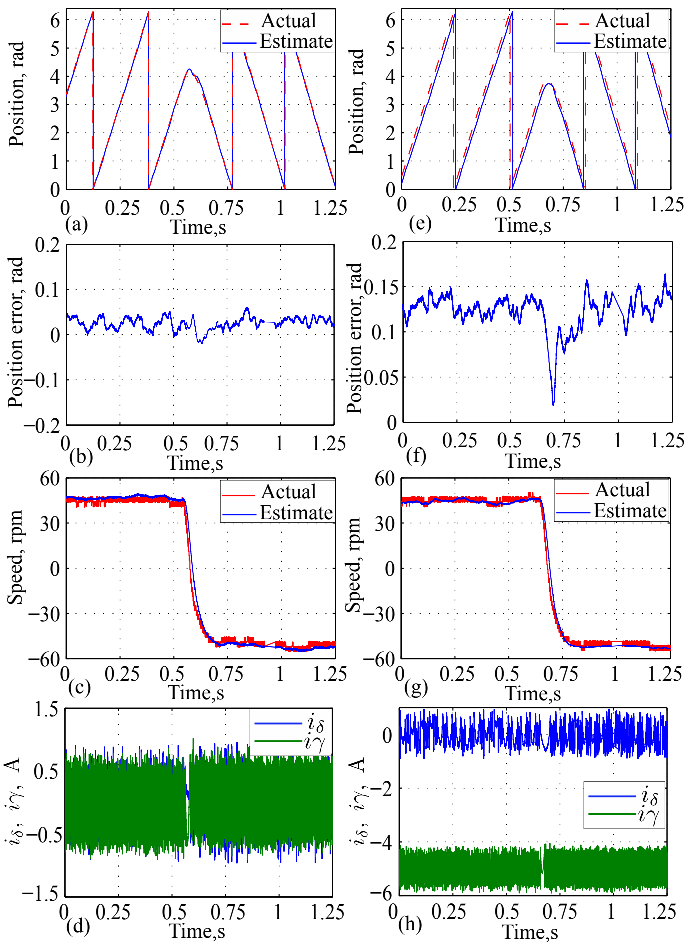

Figure 10. Experimental speed reversal performance of sensorless FCSMPC at 50 rpm: (a)-(d) at no load, and (e)-(h) at 50% rated load.

The steady state position error at higher loads for the nonlinear optimization based sensorless vector control reduces considerably with increase in the speed as the back emf component becomes dominant [21]. The steady state position error at 100 rpm and half the rated load for the nonlinear optimization based sensorless vector control is 0.08 rad (see Fig. 11(f)) which is 0.05 rad smaller as compared to the sensorless FCSMPC at the same operating condition (Fig. 12(b)). The current dynamic component is prominent as compared to the back emf term for the case of FCSMPC at 100 rpm due to the presence of high frequency switching ripples, and therefore the steady state error due to the core saturation appears. On the other hand, the switching ripples with FCSMPC helps

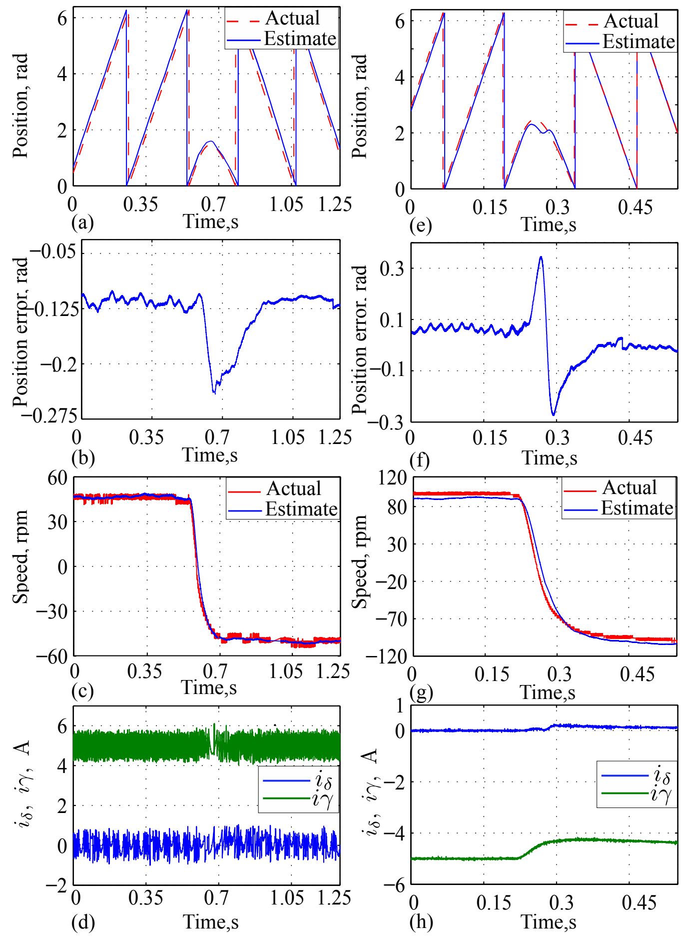

Figure 11. Experimental speed reversal performance at 50% rated load: (a)-(d) for sensorless FCSMPC with transition from motoring to generation at 50 rpm, and (e)-(h) for sensorless vector control at 100 rpm.

to improve the transient performance at the speed reversals by maintaining the observability at lower speed as compared to the sensorless vector control as shown in Fig. 11(f) and Fig. 12(b). The back emf term becomes dominant over the current dynamic component at 200 rpm for the FCSMPC and therefore the position error decreases by 0.06 rad as shown in Fig. 12(f) as compared to 100 rpm in Fig. 12(b). The position error is smooth at 200 rpm as compared to the lower speeds as the effects of current measurement noise reduces with increase in the back emf. Moreover, the current is steady at the speed transition for the case of FCSMPS as it has inherently fast response as compared to the vector control.

The steady state position error at the full rated load is increased by 0.105 rad as shown in Fig. 13 (a-b) as compared to the half rated load. However, that for the full load to 150% rated load, it is increased by only 0.05 rad as shown in Fig. 13(e-f). This shows that at 150% rated load the core is close to the complete saturation and the sensorless FCSMPC is stable with a large variations in the inductance.

The speed sweep from standstill to half the rated speed (350 rpm) and back within 150 ms are conducted to validate the performance of the nonlinear optimization based sensorless FCSMPC subjected to large speed transients. The results with

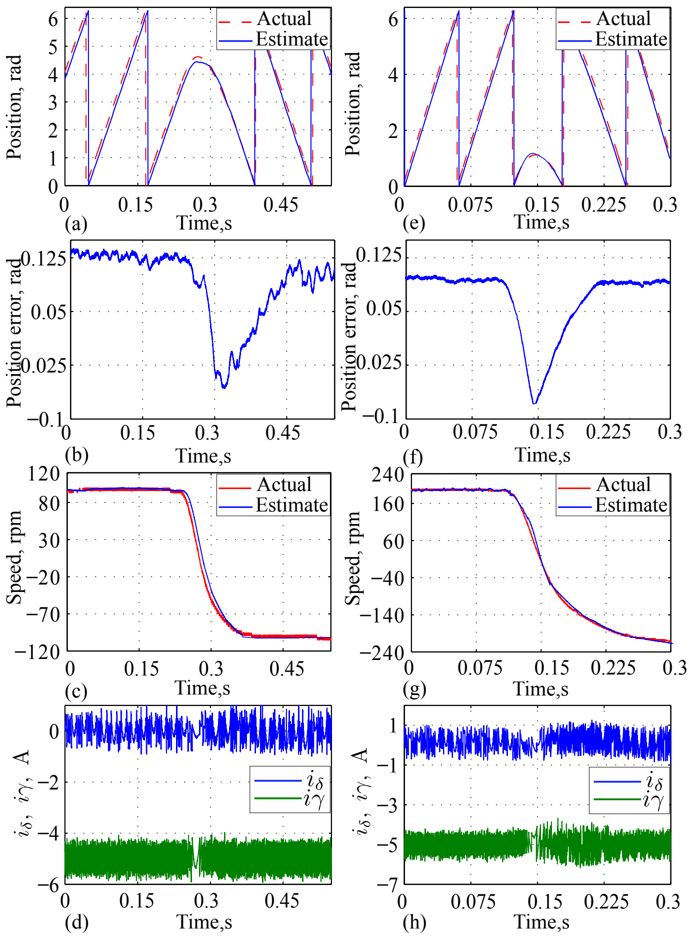

Figure 12. Experimental speed reversal performance of sensorless FCSMPC at 50% rated load: (a)-(d) at 100 rpm, and (e)-(h) at 200 rpm.

25% rated load are presented in Fig. 14 (a-d) for the FCSMPS and in (e-f) for the vector control. The reference δ axis current to produce the persistent excitation at standstill as mentioned in section VI A is not required for this case as the γ axis reference current is set at -2.5 A to produce the torque. On the other hand, a 500 Hz and 70 V sinusoidal injection is applied for the vector control till 50 rpm. The position error at the standstill for FCSMPC is 0.03 rad which is same as the no load case and that means that the core is not saturated at 25% rated load. The standstill position error for the vector control is 0.075 rad which is close to the value presented in [21]. The low standstill position error for the FCSMPC attributes to the large switching ripples. The position errors at the transient state for both the control methods are close except 0.05 rad reduction in the peak value when the speed rises for the FCSMPC as compared to the vector control.

The experimental validation of proposed sensorless scheme at very high speed (say >10000 rpm) is limited by the speed rating (700 rpm) of the reference machine. However, the proposed scheme can also be applied to high speed machine by retuning the parameters. High value of the regularization constants (κ_1 and κ_2) deteriorates the estimation at very high speed and therefore the values need to be retuned. The speed dependent machine parameters viz., winding resistance and core loss also influence the estimation performance at very high speed. The variation of the winding resistance has less significance on the estimation accuracy as discussed in section VI D, and the influence of the core loss is kept out of the scope from the present paper as it requires an elaborate treatment of the IPMSM model.

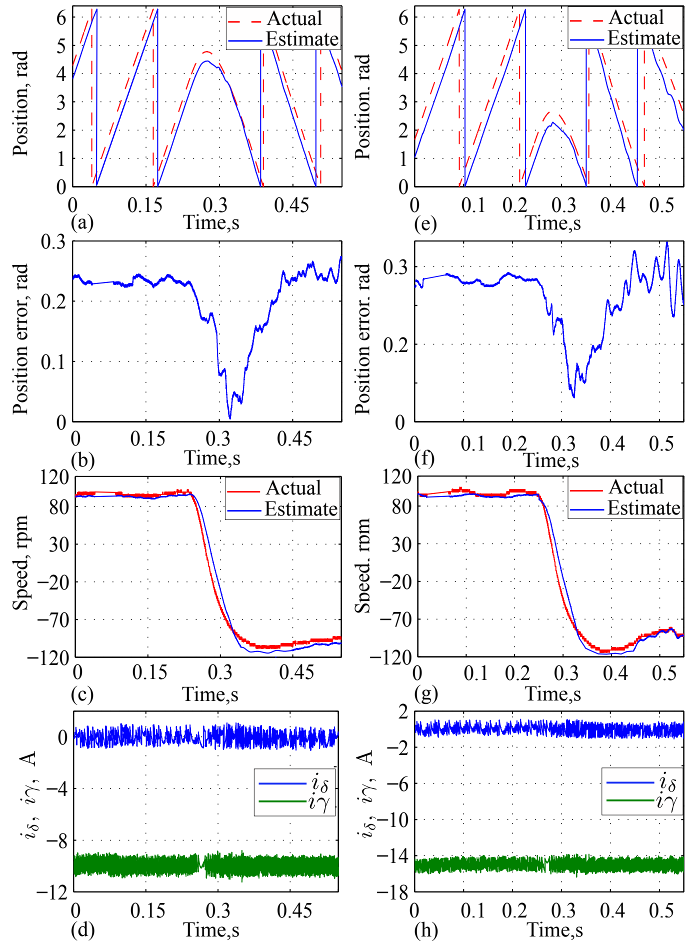

Figure 13. Experimental speed reversal performance of sensorless FCSMPC at 100 rpm: (a)-(d) at the full rated load, and (e)-(h) at 150% of the rated load.

C. *Torque Transient Performance*

The torque reversal tests are conducted to validate the transient performance of the nonlinear optimization based sensorless FCSMPC for the large torque variations. The tests results at 100 rpm and the full rated load for the FCSMPC are compared with the vector control in Fig. 15. The steady state position error for the FCSMPC is close to the vector control. The reduction in position error due to high back emf for the vector control at the half rated load as shown in Fig. 11 (f) is not observed for the full load. The high current associated with the full rated load surpasses the influence of high back emf. The position errors at the transient state for the FCSMPC and the vector control are also very close except 0.05 rad reduction in peak value for the FCSMPC.

The summary of the important experimental results are

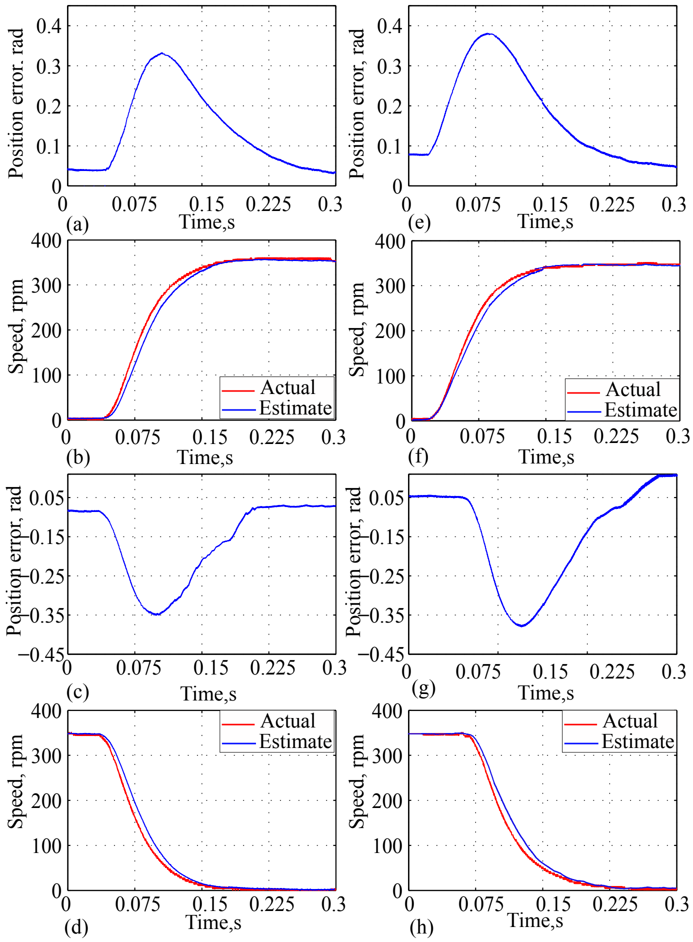

Figure 14. Experimental speed sweep performance from 0 rpm to half the rated speed (350 rpm) and back at 25% rated load: (a)-(d) for sensorless FCSMPC, and (e)-(h) for sensorless vector control.

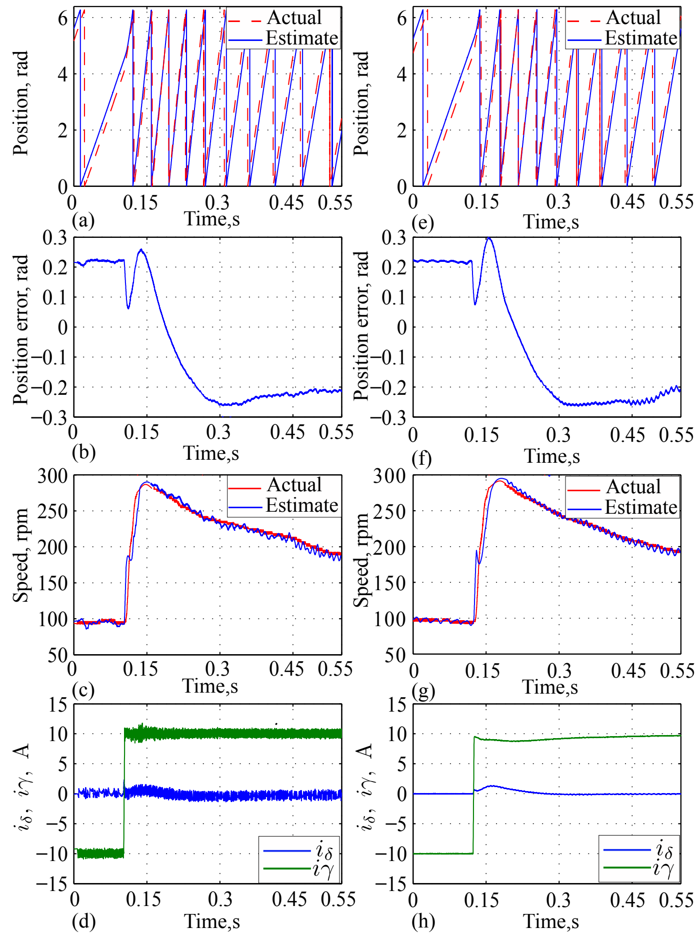

Figure 15. Experimental torque reversal performance at the full rated torque and 100 rpm: (a)-(d) for sensorless FCSMPC, and (e)-(h) for sensorless vector control.

provided in Table II for both nonlinear optimization based FCSMPC and vector control.

Table II
SUMMARY OF EXPERIMENTAL RESULTS

Operating conditions	Steady state position error (rad)		Maximum transient state position error (rad)		Response time (s)	
	FCSMPC	Vector	FCSMPC	Vector	FCSMPC	Vector
No load[1]	0.03	0.075	-	-	-	-
Speed reversal[2]	0.125	0.08	0.25	0.32	0.18	0.18
Speed sweep[3]	0.03	0.075	0.32	0.38	0.24	0.27
Torque reversal[4]	0.23	0.23	0.25	0.25	0.36	0.45

1: 50 rpm, 2: 100 rpm and 50% rated load, 3: 0 rpm to 350 rpm at 25% rated load, 4: 100 rpm with rated load.

D. Parameter Sensitivity Analysis

The nominal motor parameter values (see Table I) are supplied to this nonlinear optimization based sensorless scheme. Therefore, the variation of the physical parameters from the nominal values can affect the accuracy of the estimated position and speed. Only the sign of the optimal speed ($\hat{\omega}_o$) is required in this sensorless scheme (to perform the compensation at standstill) and hence its accuracy with respect to the parameter variations is not presented here. The position error with respect to the variations in the parameters is presented in Fig. 16 for 100 rpm with torque reversal at half the rated load. These variations are made on the nominal values supplied to the cost function to mimic the difference between the model and physical values with the actual parameter variations. The variations from the nominal values in resistance and permanent magnet flux linkage by $\pm$ 50% and $\pm$ 25% respectively do not have any significant effects on the position error as shown in Fig. 16 (a) and (c) respectively. The effect of a decrease in d axis inductance by 25% is negligible whereas an increase by 25% rises the position error by 0.025 rad with respect to the nominal case as shown in Fig. 16 (b). The decrease by 25% in q axis inductance increases the position error by 0.05 rad from the nominal case while the increase by 25% results in large oscillations apart from 0.025 rad decrease from the nominal case as shown in Fig. 16 (d). The variation in q axis inductance has the most considerable impacts on the position error as compared to other parameters. However, the position estimation by nonlinear optimization shows robustness with these large parameter variations.

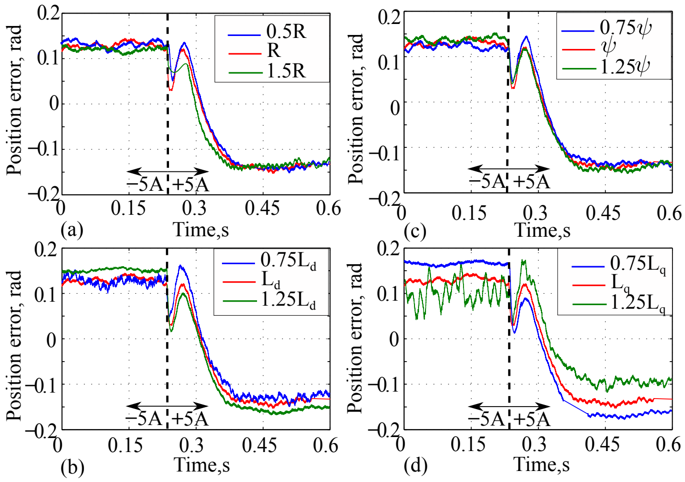

Figure 16. Position error with respect to parameter variations: (a) $\pm 50\%$ variation in resistance, (b) $\pm 25\%$ variation in d axis inductance, (c) $\pm 25\%$ variation in permanent magnet flux linkage, and (d) $\pm 25\%$ variation in q axis inductance.

VII. Conclusion

This paper presents the nonlinear optimization based position estimation scheme for IPMSM drive with FCSMPC. It shows that the proposed method is an ideal solution for drives with arbitrary signal injection- a case for FCMPC which always has inherent switching ripples due to voltage vector injection. The detailed convergence analysis is presented and developed the analytical expressions based on the leading principle minors of Hessian of the cost function to find the conditions for the convex region. This paper proposes a compensator designed based on the characteristics of the cost function to correct the wrong convergences to the saddle and symmetrical solutions. The experimental results from the speed and torque transient tests are promising and those are in par with the results from the tests conducted for the vector control with the same sensorless scheme. There is an improvement in steady state position error (by 0.045 rad) at standstill as compared to the vector control attributed to the strong switching ripples associated with FCSMPC. However, the performance of the sensorless FCSMPC deteriorates at medium speed with load (0.06 rad rise in position error) as the high switching ripples intensify the effect of inductance variation by saturation. Moreover, the proposed sensorless scheme for FCSMP performs superior as compared to other model based techniques in literature for model predictive controls. The proposed scheme has very low steady state position oscillations about ± 0.025 rad and the position error is 0.03 rad at no load and 0.225 rad at the full rated load. The future work of this paper will be focused on reducing the position error due to the parameter variations by incorporating parameter estimation.

References

[1] T. Geyer, “Generalized model predictive direct torque control: Long prediction horizons and minimization of switching losses,” in *Proc. 48th IEEE Conf. Decision and Control*, Shanghai, 2009, pp. 6799-680467996804.

[2] M. Preindl et al., “Model Predictive Torque Control with PWM using fast gradient method,” in *28^{t}h Annu. IEEE Applied Power Electronics Conf. and Expo.*, Long Beach, CA, 2013, pp. 2590-2597.

[3] M. Preindl and S. Bolognani, “Comparison of direct and PWM model predictive control for power electronic and drive systems,” in *28th Annu. IEEE Applied Power Electronics Conf. and Expo.*, Long Beach, CA, 2013, pp.25262533.

[4] T. Geyer, “Computationally Efficient Model Predictive Direct Torque Control,” *IEEE Trans. Power Electron.*, vol. 26, no. 10, pp. 2804-2816, Oct. 2011.

[5] T. Geyer, “Model Predictive Direct Torque Control: Derivation and Analysis of the State-Feedback Control Law,” *IEEE Trans. Ind. Appl.*, vol. 49, no. 5, pp. 2146-2157, Sept.-Oct. 2013.

[6] G. Papafotiou et al., “Model Predictive Direct Torque ControlPart II: Implementation and Experimental Evaluation,” *IEEE Trans. Ind. Electron.*, vol. 56, no. 6, pp. 1906-1915, June 2009.

[7] M. Preindl and S. Bolognani, “Model predictive direct speed control with finite control set of PMSM-VSI drive systems,” in *Workshop on Predictive Control of Electrical Drives and Power Electronics,* Munich, 2011, pp. 17-23.

[8] M. Preindl and S. Bolognani, “Model predictive direct torque control with finite control set for PMSM drive systems, Part 1: Maximum torque per ampere operation,” in *IEEE Trans. Ind. Informat.*, vol. 9, no. 4, pp. 1912-1921, Nov. 2013.

[9] Vaclavek et al., ”AC Drive Observability Analysis”, in *IEEE Trans. Ind. Electron.*, vol. 60, no. 8, pp. 3047-3059, Aug. 2013.

[10] L. M. Gong and Z. Q. Zhu, “Robust Initial Rotor Position Estimation of Permanent-Magnet Brushless AC Machines With Carrier-Signal-Injection-Based Sensorless Control,” in *IEEE Trans. Ind. Appl.*, vol. 49, no. 6, pp. 2602-2609, Nov.-Dec. 2013.

[11] M. J. Corley and R. D. Lorenz, “Rotor position and velocity estimation for a salient-pole permanent magnet synchronous machine at standstill and high speeds,” in *IEEE Trans. Ind. Electron.*, vol. 34, no. 4, pp. 784-789, Jul/Aug 1998.

[12] R. Leidhold, “Position Sensorless Control of PM Synchronous Motors Based on Zero-Sequence Carrier Injection,” in *IEEE Trans. Ind. Electron.*, vol. 58, no. 12, pp. 5371-5379, Dec. 2011.

[13] G. Foo and Z. Xinan, “Sensorless stator flux observer for direct torque controlled interior permanent magnet synchronous motor drives using the current derivative approach,” in *IECON 41st Annu. Conf.IEEE Industrial Electronics Society,* Yokohama, 2015, pp. 001843-001848

[14] J. B. Bartolo et al., “Flux position estimation using current derivatives for the sensorless control of AC machines,” in *3rd Int. Symposium on Communications, Control and Signal Processing,* St Julians, 2008, pp. 1468-1473.

[15] S. Nalakath et al., “Low speed position estimation scheme for model predictive control with finite control set,” in *IECON 42nd Annu. Conf. IEEE Industrial Electronics Society,* Florence, 2016, pp. 2839-2844.

[16] V. Muzikova et al., “Finite control set MPC with high frequency injections for sensorless position and speed estimation of a PMSM,” in *2015 IEEE Int. Symp. on Predictive Control of Electrical Drives and Power Electronics (PRECEDE)*, Valparaiso, 2015, pp. 9-14.

[17] M. Preindl and E. Schaltz, “Sensorless Model Predictive Direct Current Control Using Novel Second-Order PLL Observer for PMSM Drive Systems,” in *IEEE Trans. Ind. Electron.*, vol. 58, no. 9, pp. 4087-4095, Sept. 2011.

[18] L. Rovere et al., “Sensorless Finite-Control Set Model Predictive Control for IPMSM Drives,” in *IEEE Trans. Ind. Electron.*, vol. 63, no. 9, pp. 5921-5931, Sept. 2016.

[19] E. Fuentes and R. Kennel, “Sensorless-predictive torque control of the PMSM using a Reduced Order Extended Kalman Filter,” in *Symp. Sensorless Control Electrical Drives,* Birmingham, 2011, pp. 123-128, 2011.

[20] P. Landsmann and R. Kennel, “Saliency-based sensorless predictive torque control with reduced torque ripple,” in *IEEE Trans. Power Electron.*, vol. 27, no. 10, pp. 4311-4320, Oct. 2012.

[21] Y. Sun et al., “Unified Wide-Speed Sensorless Scheme Using Nonlinear Optimization for IPMSM Drives,” in *IEEE Trans. Power Electron.*, vol. 32, no. 8, pp. 6308-6322, Aug. 2017.

[22] M.A. Epelman, (2007) *IOE 511/Math 652: Continuous Optimization Methods*. Available: http://www.cse.iitd.ernet.in/ naveen/courses/CSL866/511notes.pdf

[23] Kulkarni Thaker Shefali, *Line Search Methods*. Available: http://www.cas.mcmaster.ca/ cs4te3/notes/LineSearchMethods.pdf

[24] Elvind Erikson, (2010) *Principal Minors and the Hessian*. Available: http://staff.guilan.ac.ir/staff/users/salahi/fckeditor˙repo/file/psd.pdf

Shamsuddeen Nalakath (S'07-M'11) received the Masters degree from the Department of Electrical Engineering, Indian Institute of Technology, Madras, India, in 2010. From 2010 to 2014, he was with the Advanced Engineering Group, M/s TVS Motor Company Ltd., India, where he worked in development of advanced electric machines for electric and hybrid vehicles. He is currently working toward the Ph.D. degree in electrical engineering at McMaster University, Hamilton, ON, Canada. His research interests include advanced high-performance electrical machines and controls for hybrid and electric vehicles.

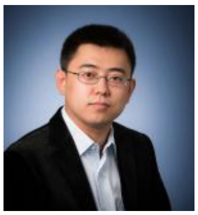

Yingguang Sun (S15-M16) received the B.S. degree in Electrical Engineering from Hebei University of Technology, Tianjin, China (2011), the M.S. degree in Electrical Engineering from Illinois Institute of Technology (IIT), Chicago, IL, USA (2013), and the Ph.D. degree from McMaster University, Hamilton, ON, Canada (2016). He is currently working as a motor control engineer at Sevcon Canada. Before joining Sevcon, he was working as a control firmware engineer at Rockwell Automation in Canada (2017). From 2013 to 2016, he was working as a research assistant for the Canada Excellence Research Chair in Hybrid Powertrain Program, Hamilton, ON, Canada. From September 2012 to June 2013, he served as a research assistant with Electric Drives and Energy Conversion Laboratory in IIT, Chicago, IL, USA. Dr. Sun obtained the best presentation prize in IECON 2015 at Yokohama, Japan. His main research areas include advanced high performance control methods for electric motor drives and power electronics applications in electrified transportation systems.

Matthias Preindl (S'12-M'15) received the B.Sc. degree in electrical engineering (*summa cum laude*) from the University of Padua, Padua, Italy, the M.Sc. degree in electrical engineering and information technology from ETH Zurich, Zurich, Switzerland, and the Ph.D. degree in energy engineering from the University of Padua, in 2008, 2010, and 2014, respectively. He was an R&D Engineer of Power Electronics and Drives at Leitwind AG, Sterzing, Italy (2010-2012), a Post Doctoral Research Associate with the McMaster Institute for Automotive Research and Technology, McMaster University, Hamilton, ON, Canada (2014-2015), and a Sessional Professor in the Department of Electrical and Computer Engineering, McMaster University (2015). He is currently an Assistant Professor in the Department of Electrical Engineering, Columbia University in the City of New York, NY, USA. He received the Career Award of the Futura Foundation in South Tyrol, Italy and the CAREER Award of the US National Science Foundation (NSF) in 2016 and 2017, respectively.

Ali Emadi (IEEE S98-M00-SM03-F13) received the B.S. and M.S. degrees in electrical engineering with highest distinction from Sharif University of Technology, Tehran, Iran, in 1995 and 1997, respectively, and the Ph.D. degree in electrical engineering from Texas AM University, College Station, TX, USA, in 2000. He is the Canada Excellence Research Chair in Hybrid Powertrain at McMaster University in Hamilton, Ontario, Canada. Before joining McMaster University, Dr. Emadi was the Harris Perlstein Endowed Chair Professor of Engineering and Director of the Electric Power and Power Electronics Center and Grainger Laboratories at Illinois Institute of Technology (IIT) in Chicago, Illinois, USA, where he established research and teaching facilities as well as courses in power electronics, motor drives, and vehicular power systems. He was the Founder, Chairman, and President of Hybrid Electric Vehicle Technologies, Inc. (HEVT) a university spin-off company of IIT. Dr. Emadi has been the recipient of numerous awards and recognitions. He was the advisor for the Formula Hybrid Teams at IIT and McMaster University, which won the GM Best Engineered Hybrid System Award at the 2010, 2013, and 2015 competitions. He is the principal author/coauthor of over 350 journal and conference papers as well as several books including Vehicular Electric Power Systems (2003), Energy Efficient Electric Motors (2004), Uninterruptible Power Supplies and Active Filters (2004), Modern Electric, Hybrid Electric, and Fuel Cell Vehicles (2nd ed, 2009), and Integrated Power Electronic Converters and Digital Control (2009). He is also the editor of the Handbook of Automotive Power Electronics and Motor Drives (2005) and Advanced Electric Drive Vehicles (2014). Dr. Emadi was the Inaugural General Chair of the 2012 IEEE Transportation Electrification Conference and Expo (ITEC) and has chaired several IEEE and SAE conferences in the areas of vehicle power and propulsion. He is the founding Editor-in-Chief of the IEEE Transactions on Transportation Electrification.